Journal of Natural Gas Science and Engineering 100 (2022) 104450

Contents lists available at ScienceDirect

Journal of Natural Gas Science and Engineering

journal homepage: www.elsevier.com/locate/jngse

Hybrid-dimensional modeling for fluid flow in heterogeneous porous media using dual fracture-pore model with flux interaction of fracture–cavity network

Luyu Wang [a,*], Weizhong Chen [c], Cornelis Vuik [b]

[a] GeoRessources Lab., UMR 7359, CNRS, 54500 Vandœuvre-lès-Nancy, France
[b] Department of Applied Mathematics, Delft University of Technology, 2628 CD Delft, The Netherlands
[c] Institute of Rock and Soil Mechanics, Chinese Academy of Sciences, 430071 Wuhan, China

ARTICLE INFO

Keywords:
Fractured porous media
Fluid flow
Heterogeneity
Discrete fractures
Natural cavity
Flux interaction

ABSTRACT

Developing numerical method of fractured porous media is of paramount importance in geoscience applications. Previous studies have revealed that the discrete fractures and cavities as well as the heterogeneity have considerable influences on hydraulic property of porous media. This work presents a numerical investigation on fluid flow in heterogeneous porous media with the consideration of flux connection of fracture–cavity network. A hybrid-dimensional modeling approach combined with the dual fracture-pore model is presented. Then, the numerical scheme is derived from Galerkin finite element method. Especially, the numerical treatment on flux interaction of multiple fractures is elaborated. Next, this model is verified by a benchmark study, and grid convergence test is performed to show the grid independence. Later, a fractured porous medium is simulated with different states of cavity. The effects of impermeable and conductive fractures on fluid flow are studied. In contrast to the homogeneous situation, we consider the effects of heterogeneity. Meanwhile, a comparison study is conducted to investigate the impacts of heterogeneity, boundary conditions and conductivity of the fracture–cavity network on fluid flow. Furthermore, pressure deviation induced by heterogeneity is analyzed with different conductivities of fractures and cavities. It appears that pressure distribution is highly related to fractures conductivity and the state of cavities, where the influence of heterogeneity on the high-conductivity fractures is relatively smaller than the low-conductivity.

1. Introduction

Simulation of fluid flow in fractured porous media is a pillar in geoscience applications, such as reservoir engineering, geothermal exploration, energy storage and waste disposal (Berkowitz, 2002; Dietrich et al., 2005), to name but a few. Discrete fractures are randomly distributed in the subsurface domain, and the size of fractures varies from fine-scale to large-scale. The heterogeneity and multiscale features produced by the discrete fractures lead to several challenges on the simulation of fluid flow (Jing, 2003; Stefansson et al., 2018) and mechanical property (Berkowitz, 2002; Wang et al., 2019b). In addition, some geological fields with complex geomorphic structures, for instance, the carbonate reservoirs, contain many natural cavities (Zhang et al., 2016; Wei et al., 2020). Therefore, these complex configurations of discrete fractures and cavities produce significant impacts on the fluid flow as well as the hydraulic-mechanical behaviors of fractured porous media. To this end, this work focuses on numerical simulation of fluid flow in heterogeneous fractured porous media, in which the flux interaction of fracture–cavity network is considered.

In practice, the hydraulic conductivity of discrete fractures is allowed to be changed in a large extent (Berkowitz, 2002; Dietrich et al., 2005). Particularly, in a subsurface aquifer with highly intersected fractures, a careful evaluation on the connectivity of fracture networks as well as the flux connection between fractures–matrix system should be addressed. These demands were initially motivated by the requirements of managing underground water resources (Cacas et al., 1990), nuclear wastes disposal (Hyman et al., 2015) and reservoir engineering (Karimi-Fard et al., 2004). In contrast to fractures, natural cavities are another special geological discontinuity encountered in field. Specially, in carbonate reservoir engineering, the cavities and fractures are connected, therefore the connected fracture–cavity system is created (Yao et al., 2010; Zhang et al., 2016; Wei et al., 2020). An important difference between cavities and fractures are the spatial extension. The width and

* Corresponding author.
E-mail addresses: wang.luyu@cnrs.fr, luyu.wang@hotmail.com (L. Wang), wzchen@whrsm.ac.cn (W. Chen), c.vuik@tudelft.nl (C. Vuik).

https://doi.org/10.1016/j.jngse.2022.104450
Received 27 July 2021; Received in revised form 1 December 2021; Accepted 25 January 2022
Available online 8 February 2022

length of a cavity are much larger than those of a fracture. It leads to different treatments on these two objects.

There are different numerical models for simulation of the flow and transport in porous media. The geological domain can be simplified as an intact medium if the effect of fractures can be neglected or fractures are absent from the region. This assumption often leads to the classical porous media model (Ababou et al., 1989; Layton et al., 2002), wherein the fluid flow is controlled by the host rock matrix. Thereafter, many improved versions have been proposed to simulate fractured media, typically the dual-porosity model (Gerke and van Genuchten, 1993; Nie et al., 2012). The transfer function is used to capture the connections of fractures and the host matrix. Furthermore, the equivalent continuum model has been developed for a highly fractured media. It is able to consider the impact of multiple fractures on fluid flow using the equivalent permeability tensor (Lang et al., 2014; Hadgu et al., 2017). Those two classical models, i.e. the porous model and the dual-porosity model, are implicitly representing each of the fractures. However, in some geoscience applications, where the large scale fractures and intersected multiple fractures widely exist, the classical models are oversimplified and inaccurate. To this end, the discrete fracture network (DFN) has been proposed (Long and Billaux, 1987; Cacas et al., 1990), such that the discrete fractures can be explicitly represented. Afterwards, many models have been developed based on DFN (Zhang and Sheng, 2021; Huang et al., 2021a; Graf and Therrien, 2008; Mustapha et al., 2011; Fumagalli et al., 2019). Nevertheless, the drawback of this model is that fluid flow is assumed only in the fracture networks, while the matrix is impermeable. It is failed to simulate a fractured medium with the consideration of flux interaction between fractures and matrix. To this end, the discrete fracture model (DFM) (Karimi-Fard et al., 2004; Stefansson et al., 2018; Sherratt et al., 2020) and embedded discrete fracture model (EDFM) (Hajibeygi and Jenny, 2011; HosseiniMehr et al., 2018; Shakiba et al., 2018), have been proposed in recent decades.

In terms of meshing strategy and the numerical discretization, DFM and EDFM have different pros and cons. The complex configuration of multiple fractures leads to a challenge of grid generation (Hyman et al., 2015). There are many research works of mesh generation focusing on the DFM-based methods, typically the efficient and fast algorithms to generate finite element meshes (Berrone et al., 2013; Hyman et al., 2014; Bahrainian et al., 2015). In this way, an efficient treatment is that the discrete fractures are considered as the relative low-dimensional objects placed on the interfaces of matrix cells. Another scheme of fracture cells is to assign an actual aperture to each fracture cell, therefore the fracture cells are actually a quadrilateral elements with very small aperture, as discussed in literature (Cappa and Rutqvist, 2011; Wang et al., 2020). This strategy also has been applied in different geoscience applications (Rutqvist et al., 2008; Wang et al., 2019a; Tan et al., 2020). Meanwhile, an alternative numerical method, EDFM, is developed, in which the grids of fractures and rock matrix are independent (Hajibeygi and Jenny, 2011; Shakiba et al., 2018). Recently, an improved version, the projection-based embedded fracture model (pEDFM) (Ţene et al., 2017), has been developed to enable the modeling of high contrast hydraulic conductivity between fractures and matrix. Afterwards, different numerical methods are widely used in geoscience applications, typically two-phase flow (Huang et al., 2021b), hydrogen storage (Ratnakar et al., 2020), CO_2 capture and process optimization (Moradi et al., 2014; Atashbeyk et al., 2018; Hosseini-Ardali et al., 2020). However, the DFM method still enjoys several attractive features and occupies an important role in reservoir simulation. The DFM solution is often selected as the reference solution to other numerical schemes. The accurate simulation of connection between the matrix and fractures can be guaranteed in the formulations of finite element and finite volume methods. It provides a basis of the presented work.

Crucially, investigation of the effects of heterogeneity and fracture–cavity network on fluid flow in fractured porous media remains importance in geoscience applications. This work focuses on numerical simulation of fluid flow in heterogeneous porous media. A hybrid-dimensional modeling approach combined with the dual fracture-pore model is presented. Moreover, the numerical treatment on flux interaction of multiple fractures is elaborated. Based on these, we study quantitatively the effects of heterogeneity and fracture–cavity network on pressure distribution. The discrete fractures and cavities are allowed to be assigned to impermeable or conductive properties.

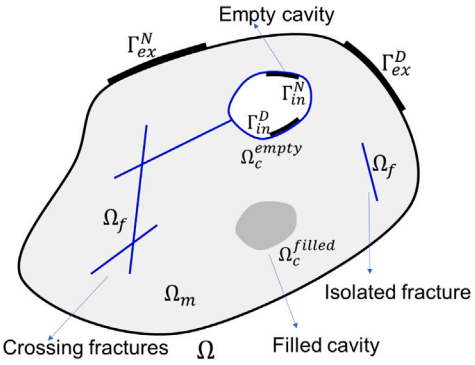

Fig. 1. A porous medium with discrete fractures and cavities.

This paper is structured as follows. First, the formulation of fluid flow in fractured porous media is presented in Section 2. Then, in Section 3, the numerical discretization of the governing equation is introduced. Especially, the numerical treatments of flux interaction of multiple fractures and the fracture–cavity network are elaborated in Section 4. Later, in Section 5, the proposed method is verified by a benchmark study. A heterogeneous fractured porous medium with different types of cavities is simulated. The effects of heterogeneity and conductivity of the fracture–cavity network on fluid flow are studied.

2. Problem description

In this section, the formulation of fluid flow in fractured reservoir is provided. The dual fracture-pore model is introduced, and combined with the discrete fracture model, to simulate a fracture reservoir with complex geometry. The domain is decomposed into the porous matrix, stochastic fractures and natural cavities.

2.1. Physical domain and dual fracture-pore model

A fractured medium with the discrete fractures and cavities is displayed in Fig. 1. The domain Ω consists of three sub-components, namely the matrix Ω_m, fractures Ω_f and cavities Ω_c:

$$\Omega = \Omega_m \cup \left(\cup_{i=1}^{N_f} \Omega_{f,i}\right) \cup \left(\cup_{j=1}^{N_c} \Omega_{c,j}\right) \tag{1}$$

where the numbers of fractures and cavities are N_f and N_c, respectively.

In a naturally fractured reservoir, Ω_f and Ω_c are stochastically distributed. Ω_f is modeled as the low-dimensional objective, and can be viewed as lines in two dimensional and surfaces in three-dimensional problems.

However, the situation is different for the cavities. Naturally, Ω_c has larger size compared with the fractures. We simulate the empty cavities Ω_c^{empty} and the filled cavities Ω_c^{filled} separately. Based on these concepts, a cavity $\Omega_{c,i}$ can be categorized as $\Omega_{c,i} = \Omega_{c,i}^{empty} \cup \Omega_{c,i}^{filled}$, as shown in Fig. 1.

The fractures and cavities may generate either a conductive channel or play the role of barrier for fluid flow. In our model, the cavities are allowed connecting and coalescing to each other. The fractures are intersected, then a fracture network is constructed, as shown in Fig. 1.

The entire boundary Γ of the domain consists of two main parts $\partial\Omega := \Gamma = \Gamma_{ex} \cup \Gamma_{in}$. The external boundary is denoted as Γ_{ex}. The

internal boundary related to the cavities and fractures is denoted as Γ_{in}.

The boundaries with Dirichlet and Neumann types are represented by Γ^D and Γ^N, respectively. Different types of boundary condition can be imposed on $\Gamma_{ex} = \Gamma_{ex}^D \cup \Gamma_{ex}^N$ or $\Gamma_{in} = \Gamma_{in}^D \cup \Gamma_{in}^N$. Note that $\Gamma^D \cap \Gamma^N = \emptyset$.

2.2. Conservation law of fluid flow

The flow equation is derived by the mass conservation law and the momentum equation (Darcy's law). For a conserved quantity q, the functions of source term f and the flux $\mathbf{F}$ are defined. We introduce the general form of conservation law (LeVeque, 1992; Eymard et al., 2000), therefore the conservation equation is valid at arbitrary spatial–temporal position $(\mathbf{x}, t)$ inside Ω:

$$q_t(\mathbf{x}, t) + \nabla \cdot \mathbf{F}(\mathbf{x}, t) = f(\mathbf{x}, t) \quad \text{on } \Omega \tag{2}$$

Considering a single phase compressible fluid with the porosity of medium ϕ, density of fluid ρ, mobility λ and source q, then applying Eq. (2) and substituting $\mathbf{F}(\mathbf{x}, t) = \rho\mathbf{u}$ and $f(\mathbf{x}, t) = \rho q$, the governing equation is written as:

$$\frac{\partial(\phi\rho)}{\partial t} + \nabla \cdot (\rho\mathbf{u}) = \rho q \quad \text{on } \Omega \tag{3}$$

where λ is related to viscosity μ and permeability $\mathbf{K}$ of the fluid. The fluid velocity $\mathbf{u}$ is expressed by Darcy's law $\mathbf{u} = -\lambda\nabla p$. In this work, the incompressible assumption is applied. Therefore, Eq. (3) is simplified as:

$$-\nabla \cdot (\lambda\nabla p) = q \quad \text{on } \Omega \tag{4}$$

Eq. (4) is an elliptic partial differential equation (PDE). To propose a well-posed boundary value problem, the boundary conditions should be given. For the elliptic PDE in flow problem, Eq. (4) is subjected to the prescribed pressures $\bar{p}$ or prescribed volumetric flux $\bar{q}$ on Γ:

$$\begin{aligned} p &= \bar{p} \quad \text{on } \Gamma^D \\ -(\lambda\nabla p) \cdot \mathbf{n} &= \bar{q} \quad \text{on } \Gamma^N \end{aligned} \tag{5}$$

where $\mathbf{n}$ is the outward unit vector of the external boundary. Especially, if a cavity is empty, the inlet boundary can be specified on the edge of cavity to model the internal pressure.

3. Numerical method

In this section, the governing equation is discretized on unstructured grids, where the local conservation of flux is ensured. The numerical scheme is derived from the Galerkin finite element method (GFEM), in which the test function is a piece-wise constant function. All algorithms are implemented in our C++ program.

3.1. Mesh partition using Delaunay algorithm

To solve the boundary value problem Eqs. (4) and (5), the geometry of the domain Ω is partitioned into discretized grids with n_{ele} non-overlapping cells, $\Omega = \cup_{i=1}^{n_{ele}} e_i$. We use a Delaunay triangulation to conduct the geometrical discretization. This method enjoys an attractive feature of flexible treatment on the complex fractured vuggy porous medium.

In Delaunay triangulation, the fractures are discretized by the relative low-dimensional cells compared to the high-dimensional matrix cells, as shown in Fig. 2. The fracture cells are arranged along the matrix cells, thereafter the scheme of conformal grids is applied. The sub-domains of filled cavities are partitioned by triangles, while the empty cavities are treated as internal boundaries. Note that each cell in the grids shares three common edges with its neighbors.

The procedure of generating low-dimensional fracture cells is presented in Algorithm 1.

Algorithm 1 Generation of low-dimensional fracture cells

Note that the number of fractures is N_f; the number of matrix cells is n_{ele}

for each $i \in [1, N_f]$ **do**
  Fracture f_i is defined by coordinate (X_i, Y_i)
  Calculate the geometrical equation of f_i according to (X_i, Y_i)
end for
for each $i \in [1, n_{ele}]$ **do**
  For matrix cell e_i^m, finding its neighbors and constructing cell pairs
  Based on geometrical equation of each fracture, creating fracture cells
end for
Counting the number of all e^f, noted as n^f
for each $i \in [1, n^f]$ **do**
  Check grid connectivity of fracture cells, classifying intersected e^f that placed on crossed-fracture positions
  Update node connectivity of intersected positions
end for

3.2. Galerkin finite element formulation

In this work, the numerical scheme is originated from Galerkin finite element method. Combining with the hybrid-dimensional model, the discretization is valid in both fractures and the matrix. The aperture of fractures is assumed as a virtual aperture in computation, as shown in Fig. 2. A discontinuous Galerkin method is then formulated.

The test function is selected as a piece-wise constant function η. Based on these, the local conservation of flux is ensured. The solution satisfies with several requirements defined by function analysis. The solution space is a subset of the square integrable function space $L^2(\Omega) = \left\{p : \int_\Omega |p|^2 \, d\Omega < +\infty\right\}$ (Jha and Juanes, 2007). Let $\mathcal{U}_h \subset L^2(\Omega)$ be the function space of solution for pressure p. The corresponding subspace for the test function η is defined as $\mathcal{U}_0$, therefore $\eta \in \mathcal{U}_0$. The aim is to find a solution $p \in \mathcal{U}_h$.

Consequently, p is approximated by the Galerkin finite element approximation (Jha and Juanes, 2007; Zienkiewicz et al., 2013):

$$p \approx p_h = \sum_{i=1}^{n_{ele}} \eta_i p_i \tag{6}$$

where η is the shape function, as illustrated in Fig. 3a. The piece-wise constant function η reads:

$$\eta_i = \begin{cases} 1 & \text{cell } i \\ 0 & \text{other cells} \end{cases} \tag{7}$$

Therefore, the shape function is defined in the framework of finite element approximation. Considering the integral over the entire domain Ω and multiplying test function η with each term in Eq. (4), the integral form reads:

$$\sum_{i=1}^{n_{ele}} \int_{\Omega_i} -\eta\nabla \cdot (\lambda\nabla p) \, dV = \int_{\Omega_i} \eta q dV \tag{8}$$

For a certain cell Ω_i, the set of edges for this cell is denoted by Γ_i. Applying Gauss theorem, the semi-discretization is expressed as:

$$\int_{\Gamma_i} -\eta(\lambda\nabla p) \cdot \mathbf{n}_\Gamma d\gamma = \int_{\Omega_i} \eta q dV \tag{9}$$

It holds valid on each cell of the grids, including matrix, fracture and cavity cells. For different types of cell, the equation has different forms. The interaction between matrix and fractures/cavities would be presented in Section 4.

3.3. Fully discretized forms

The numerical scheme can be applied to grids with arbitrary polygons. In this work, we consider the triangular cells due to the commonly used unstructured grids. Note that the number of edges of cell i is Γ_i,

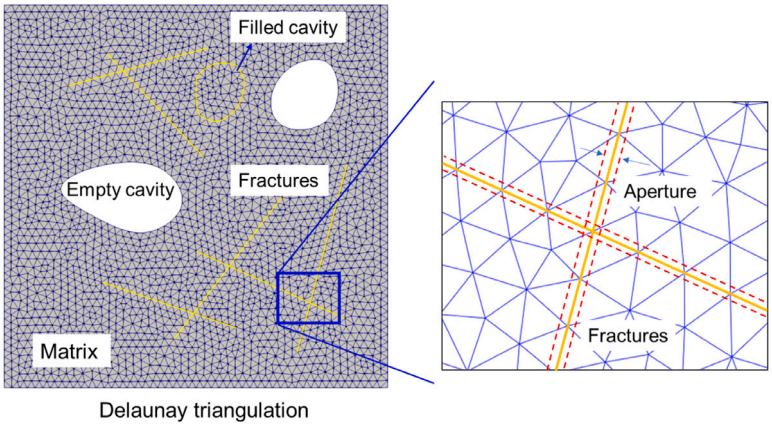

Fig. 2. Schematic of mesh partition. Fractures are discretized as the interfaces along matrix cells. Cavities are regarded as internal constrained boundaries. The virtual aperture is assigned to each fracture cell.

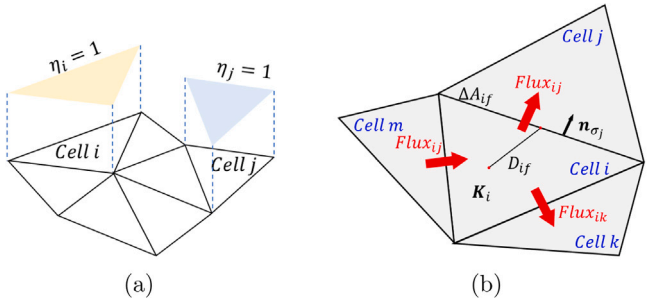

Fig. 3. (a) Schematic of shape function. (b) Cell parameters used in numerical discretization.

and one of the edges is denoted by σ_*. The number of neighbors of cell i is $n_{eighs,i}$. We have the expression:

$$\sum_{*=j,k,m}^{n_{eighs,i}} \int_{\sigma_*} -\eta\,(\lambda \nabla p)\cdot \mathbf{n}_{\sigma_*}\, d\gamma = \int_{\Omega_i} \eta q dV \tag{10}$$

where $\mathbf{n}_{\sigma_*}$ is the normal vector that points to the outward of the edge σ_* belonging to cell Ω_i, as displayed in Fig. 3b.

Applying the cell-central formulation, which is widely used in reservoir simulation, the fully discretized formula reads:

$$\sum_{*=j,k,m}^{n_{neigh,i}} T_{i*}\left(p_i - p_*\right) = q_i \Delta V_i \tag{11}$$

The coefficient $T_{i*} = \left(T_{if} T_{*f}\right) \Big/ \left(T_{if} + T_{*f}\right)$ is defined by the expression:

$$T_{if} = \frac{\Delta A_{if}\left(\mathbf{n}_{\sigma_*}\cdot\left(\mathbf{K}_i\cdot\mathbf{n}_{\sigma_*}\right)\right)}{D_{if}\mathbf{n}_{\sigma_*}} \tag{12}$$

where ΔA_{if} is the area of the face between cell i and its neighbor cell $*$. D_{if} is the distance from cell-center of cell i to the central point at the edge shared with neighbor cell $*$, as shown in Fig. 3b. $\mathbf{K}_i$ is the permeability tensor of cell i. Note that $*= j,k,m$ when the polygonal cell is a triangle.

According to the mass conservation law $\nabla\cdot\mathbf{u} = q$, the flux can be calculated:

$$q_i \Delta V_i = \sum u_{i*}\Delta A_{i*} \tag{13}$$

Consequently, the flux at each interface of cell i can be calculated. It indicates that the total flux of a cell is the summation of sub-flux at each interface, as illustrated in Fig. 3b.

3.4. Algebraic system considering fracture–cavity network

The preceding formulation proposes the well-posed boundary value problem, and then it is discretized using the Galerkin finite element formulation. The solution is computed based on the algebraic system, which is constructed by the discretized formulas Eqs. (11) and (12).

Once the coefficient T_{i*} is calculated for all connections of matrix–matrix, matrix–fractures and fractures–fractures, we can then construct the integrated algebraic system $\mathbf{C}_{n_{ele}\times n_{ele}}\mathbf{p}_{n_{ele}\times 1} = \mathbf{q}_{n_{ele}\times 1}$, by assembling T_{i*} of each cell according to the grid connectivity:

$$\begin{bmatrix} \mathbf{C}_{mm} & \mathbf{C}_{mf} & \mathbf{C}_{mc} \\ \mathbf{C}_{fm} & \mathbf{C}_{ff} & \mathbf{C}_{fc} \\ \mathbf{C}_{cm} & \mathbf{C}_{cf} & \mathbf{C}_{cc} \end{bmatrix} \begin{bmatrix} \mathbf{p}_m \\ \mathbf{p}_f \\ \mathbf{p}_c \end{bmatrix} = \begin{bmatrix} \mathbf{q}_m \\ \mathbf{q}_f \\ \mathbf{q}_c \end{bmatrix} \tag{14}$$

where $\mathbf{C}_{\alpha\alpha}$ on the diagonal represents the sub-block related to interaction of matrix/fracture/cavity cells with itself. $\mathbf{C}_{\alpha\beta}$ on the off-diagonal is the interaction of matrix–fractures/cavities, fractures–cavities/matrix. Note that the subscripts m, f, c are matrix, fractures and cavities, respectively. Therefore, $\alpha, \beta = m, f, c$ and $\beta \neq \alpha$.

4. Flux interaction of multiple fractures

Eqs. (11) and (12) are the unified formulas of the cells of matrix, fractures and cavities. However, when applying these formulas to simulate fluid flow in fractured reservoir, several difficulties appear. To this end, the flux connection of multiple fractures needs a special treatment.

4.1. Connections of matrix, fractures and cavities

It is useful to classify different types of matrix cells and fracture cells. The grid connectivity, which is given by the Delaunay algorithm in Section 3.1, plays an important role in this consideration, where the requisite information of topological connectivity of cells is provided.

As illustrated in Fig. 4, each of the low-dimensional fracture cells has two types of neighbors, the matrix and fractures cells. In Section 2, the filled cavities and empty cavities are defined, which have different hydraulic properties. (1) In the former case, it can be viewed as special type of matrix, but has significant different values of permeability compared to the matrix. (2) Conversely, the later case is often considered as the internal boundary, such that it can be assigned as inlet or outlet boundary.

Based on these, the interactions of matrix, fractures and cavities are mainly classified as two groups:

- Group 1: The flux in matrix cells allows exchange with both cavities and fracture cells, including matrix ⇔ matrix, matrix ⇔ filled cavities, matrix ⇔ fractures.

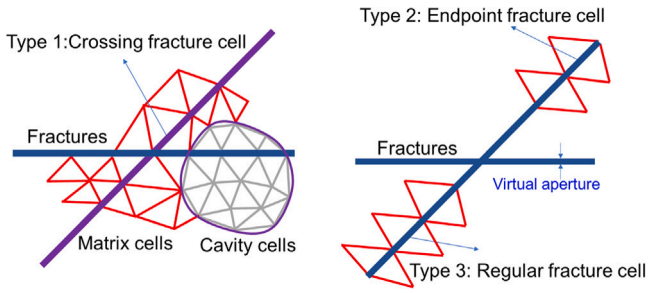

Fig. 4. Different types of interaction of fractures–matrix and fractures–fractures. .

- Group 2: The flux in fractures and cavities allows exchange, including fractures ⇔ fractures, filled cavities ⇔ filled cavities, fractures ⇔ filled cavities.

The interactions in Group 1 are directly treated by the use of the standard GFEM, as presented in Section 3, while the permeability of filled cavities allows different from that of matrix. However, the situation is totally different in Group 2, since the low-dimensional fracture cells lead to the difficulty of topological connection to the high-dimensional matrix cells.

Algorithm 2 Procedure for treatment of matrix, fractures and cavities

1: **for** each $i \in [1, n_{ele}]$ **do**
2: Cell e_i is classified as cells of matrix e_i^m, fracture e_i^f or cavity e_i^c
3: Classifying e_i, where number of e^m, e^f and e^c are denoted as n^m, n^f and n^c
4: **end for**
Note that $n_{ele} = n^m + n^f + n^c$, $e_i = e^m \vee e^f \vee e^c$
5: **for** each $i \in [1, n^m]$ **do**
6: Cell e_i^m has three neighbors for non-boundary cells, and one or two neighbors for boundary cells
7: Find all neighbors of each e_i^m, which is stored in the data structure
8: Calculating T_{i*} according to neighbors of e_i^m
9: **end for**
10: **for** each $i \in [1, n^f]$ **do**
11: Cell e_i^f can be classified as different types based on the discussion in Section 4.2
12: Different types of crossing fractures is identified
13: Calculating T_{i*} according to e_i^f and its neighbors.
14: Eqs. (12) and (15) are used to calculated T_{if} for matrix and fracture
15: **end for**
Repeat Lines 5 to 9 for cavity cells from 1 to n^c

4.2. Connection of multiple fractures

The flux exchanges at the crossing position of multiple fractures allows several directions, as shown in Fig. 4. The flow direction is determined by the pressure gradient ∇p of each cell pair. Therefore, the efficient star-delta procedure is applied to avoid the computational expansive and numerical instability (Karimi-Fard et al., 2004). The original motivation of the procedure originated from a renormalization technique for calculating the permeability of heterogeneous media (King, 1989). To this end, it is important to categorize the fracture cells as follows:

- Type 1: Fracture cell at the intersection has six neighbors, including four fracture cells and two matrix cells.
- Type 2: Fracture cell at the endpoint has three neighbors, including two matrix cells and one fracture cell.
- Type 3: The regular fracture cell has four neighbors, including two matrix cells and two fracture cells.

In the presented method, each fracture cell is assigned to an aperture, as illustrated in Fig. 4. Note that the aperture is a virtual value that evaluated in computational consideration instead of a real physical width. In this context, Eq. (12) is adopted to calculate the fracture–fracture interaction:

$$T_{if}^{frac} = \frac{\Delta a_i \left(\mathbf{t}_i \cdot \left(\mathbf{K}_i \cdot \mathbf{t}_i\right)\right)}{L_i} \tag{15}$$

where Δa_i and L_i are the aperture and half length of fracture cell, respectively. $\mathbf{t}_i$ is the unit vector in the tangential direction of the fracture. Therefore, the fluid fluxes of the low-dimensional cells (fractures) and high-dimensional cells (matrix and cavity cells) are calculated in different situations, as shown in Algorithm 2.

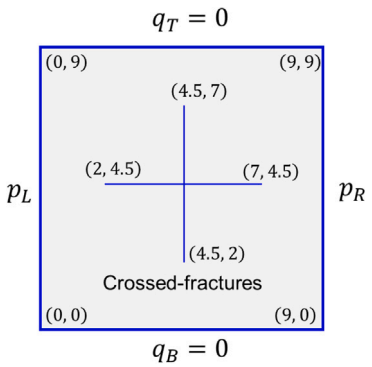

Fig. 5. Schematic of the crossed-fractures model. .

5. Numerical results and discussion

Numerical tests are carried out in this section using the presented numerical method. This method is verified by a classical benchmark study. Grid convergence is evaluated with different grid resolutions. Then, a fractured porous medium with different geometrical configurations is simulated under different conditions. The effects of hydraulic conductivity, cavities and heterogeneity on fluid flow in fractured reservoir are analyzed.

5.1. Numerical validation and grid convergence

Before applying the presented numerical method to simulate a heterogeneous fractured reservoir with complex geometry, the validation and convergence evolution should be performed. The model used for benchmark, namely the crossed-fractures model, is given in literature (Hajibeygi et al., 2011; Ţene et al., 2017). The geometrical configuration is shown in Fig. 5. Note that the size of the domain is 9 m × 9 m. The crossed-shape fractures, each one with length 5 m, are placed on the center of the domain. To fully resolve the model with a very fine grid resolution, the fracture aperture $\Delta a = 5 \times 10^{-3}$ m approximates to the grid resolution.

The homogeneous assumption is adopted, as given in literature (Hajibeygi et al., 2011; Ţene et al., 2017). The permeability of rock matrix is set to $k_m = 10^{-12}$ m^2. The permeability of fractures k_f is determined by the permeability ratio $k_r = k_f/k_m$, which reflects the difference of hydraulic property between matrix and fractures. We assign the ratio $k_r = 10^5$ and 10^{-5} to simulate the conductive channel and the barrier for fluid flow, respectively. The pressure boundary condition is imposed on the left boundary $p_L = 1$MPa, while the outlet is placed at the right boundary. The top and bottom boundaries are impermeable, as shown in Fig. 5.

Boundary conditions, as well as the conductivity of fractures, would influence fluid flow in the fractured medium. Fig. 6a shows the pressure distribution in the case of crossed-fractures with high-conductivity. Simulation results agree well with the results reported in literature (Hajibeygi et al., 2011; Ţene et al., 2017). It appears that the presence

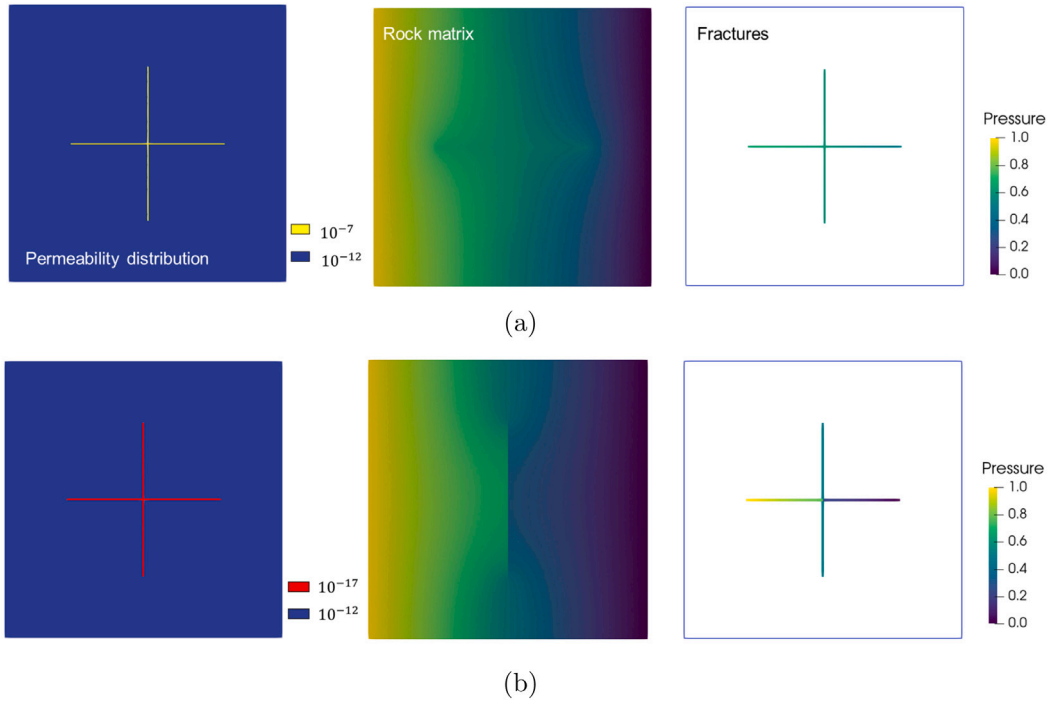

Fig. 6. Permeability (unit: [m^2]) and pressure distribution (unit: [MPa]) for matrix and fractures. (a) High-conductivity of the crossed-fractures leads to a conductive pathway. (b) Low-conductivity produces the blocking effect.

of fractures produces a conductive pathway for fluid flow, therefore fluid directly flows through the pathway. Pressure distribution shows a slight influence induced by the fractures. Fig. 6b provides a contrasting comparison, in which the low-conductivity of fractures is considered. The fractures play the role of a barrier for fluid flow, therefore the discontinuity of pressure can be observed. In addition, pressure distribution over the crossed-fractures is totally different in these two situations. The blocking fractures lead to a higher pressure magnitude than the high-conductivity fractures, as displayed in Fig. 6b.

To evaluate the convergence performance of the proposed numerical method, grid convergence test is conducted. The reference solution is denoted as $\{P_i\}$. The results calculated by different grid resolutions h, denoted as $\{p_i^h\}$, are compared with the reference solution. It is useful to define the error percentage to evaluate the performance of grid convergence:

$$\epsilon^h = \sum_{i=1}^{N_p} \frac{\left\| P_i - p_i^h \right\|_2}{\left\| P_i \right\|_2} \tag{16}$$

where N_p is the number of cells along the diagonal of the domain.

As displayed in Fig. 7, different grid resolutions are selected for testing the grid convergence. A comparison of the results simulated by different methods is provided. The error of different solutions ϵ^h measured by Eq. (16) is reduced with the increased grid resolution. It proves that the proposed numerical method is grid-independent and it has at least first-order accuracy. Fig. 8 illustrates an example that a comparison between the fully-resolved solution and solutions with two different levels of refinement. It shows that the relative coarse resolution is able to reproduce the same result compared to the fine resolution.

5.2. Sensitivity to the hydraulic conductivity of fractures and matrix

In practice, the matrix and fractures are often naturally assigned to different conductivities. Normally, the rock matrix has relative low-permeability compared to the fractures. In contrast, the fractures can also exhibit a barrier effect instead of the conductive channels due to the geological environment. Therefore, we analyze the pressure distribution on fractures with different permeabilities to show the impacts of impermeable or conductive fractures. The parameters are same as in the above test.

Fig. 9 illustrates pressure distribution in different situations. The permeability ratio is set to $k_r = 10^5$ and 10^{-5}. It indicates that the barrier effect of fractures produces a significant discontinuity in the pressure field. The movement of fluid is blocked around the low-conductivity fractures. Furthermore, the type of boundary conditions, specifically the injection position, also affects the pressure distribution. To this end, we consider different injection types. As displayed in Fig. 9a, the horizontal fracture is inactive if the injection is imposed on the entire left surface. While if the injection is applied on the left bottom corner, as shown in Fig. 9c, both horizontal and vertical fractures are active. In the situation of high-conductivity fractures, the pressure distribution shows a slight perturbation only in the region around fractures, which can be seen in the contour maps of Figs. 9b and d. Comparing the pressure distributions calculated by different permeabilities, it is concluded that the pressure gradient is very high around the fracture network if it plays the role of barriers. The pressure concentration would disappears if the fractures are assigned to high-conductivity.

The pressure distribution along fractures strongly depends on the hydraulic properties of fractures and rock matrix. Specifically, in the crossed-fractures model, the horizontal and vertical fractures show obviously different behaviors. A set of curves, corresponding to Fig. 9, to show pressure distribution along the horizontal and vertical fractures under different situations, are illustrated in Figs. 10 and 11. It appears that a significant jump around the horizontal fracture when this fracture plays the role of flow barrier, as depicted in Fig. 10a, corresponding to Fig. 9a. If the injection is placed on the left bottom corner, the discontinuous pressure is observed in both the horizontal and vertical fractures, as shown in Fig. 10b.

Fig. 11 demonstrates that pressure on the horizontal fracture shows a linear decay if the fracture is assigned to high-conductivity ($k_r = 10^5$). The reason is that the fracture plays the role of conductive pathway, which directly conducts the fluid from inlet to outlet, therefore fluid

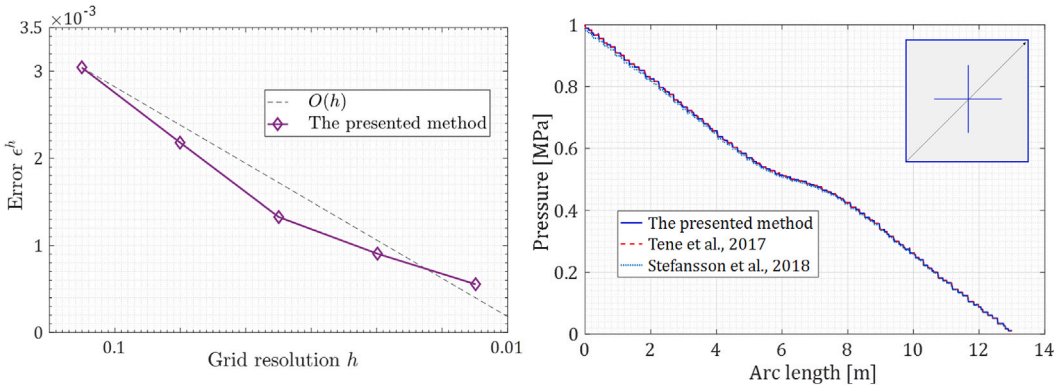

Fig. 7. Grid independence test (left) and comparison of the results calculated by different methods (right).

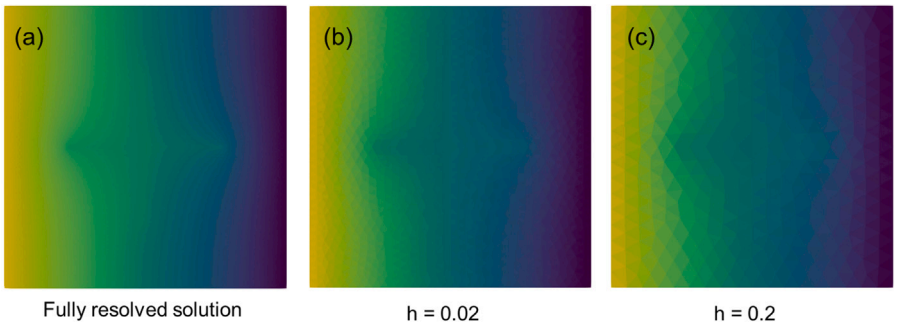

Fig. 8. Comparison of the results calculated by different grid resolutions. (a) The fully-resolved solution. (b) and (c) are discretized by 7512 and 4274 cells, respectively.

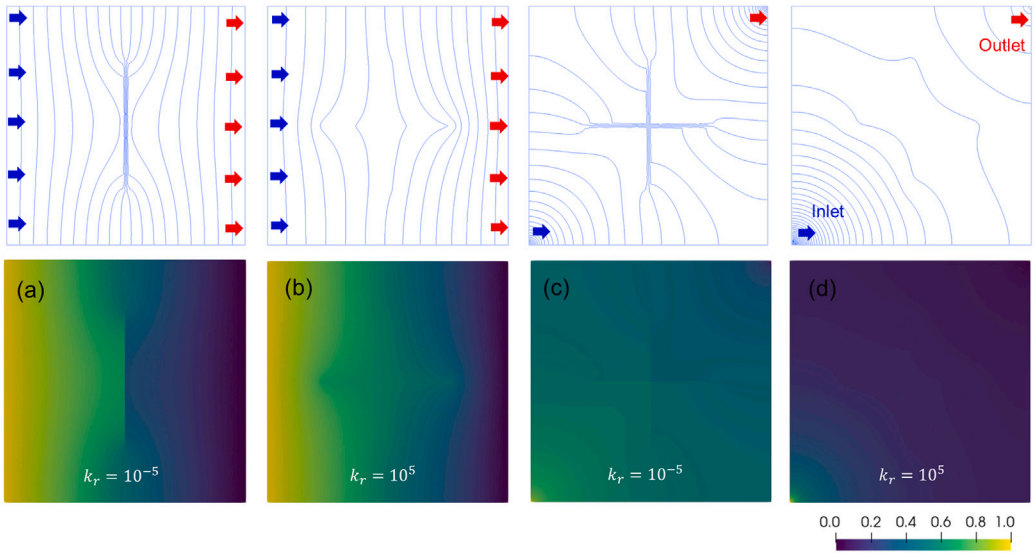

Fig. 9. Pressure distribution expressed by contour maps (top) and profiles (bottom). The injection position and permeability are allowed to be changed.

flow in the horizontal fracture produces a linear pressure gradient. Note that when the injection is imposed on the left bottom corner of the domain, both horizontal and vertical fractures exhibit the same behavior, since the symmetric effect of fluid flow in the crossed-fractures, as shown in Fig. 11b.

5.3. Flow in fractured porous media with cavities

A fractured porous medium with different types of cavities is simulated with the consideration of flux connection in fracture–cavity network. The discrete fractures and cavities are stochastically distributed inside this medium. The multiple crossing fractures are considered, while the empty cavity and filled cavity are connected through the pathways generated by the discrete fractures. Especially, the filled cavity is allowed to be assigned to a different hydraulic conductivity k_c compared to the rock matrix k_m, therefore it creates a barrier or conductive pathway to fluid flow.

The domain is a square with size 100 m × 100 m, as shown in Fig. 12. To study the effects of cavities, as well as the permeability of cavities and fractures, we consider three different patterns of this model. Different permeabilities and boundary conditions are given in Table 1. Note that in Patterns A and B, the permeability of filled

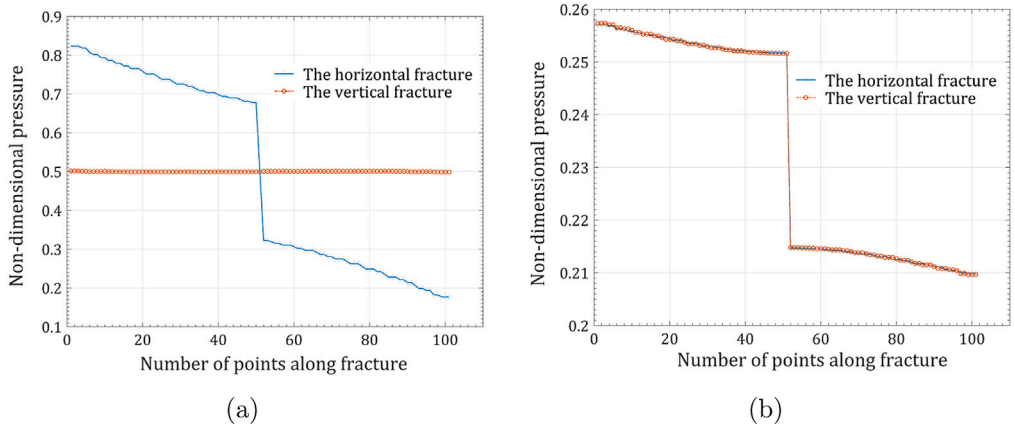

Fig. 10. Pressure variation along fractures when fractures are impermeable ($k_r = 10^{-5}$). Note that (a) and (b) correspond to Figs. 9a and 9c, respectively.

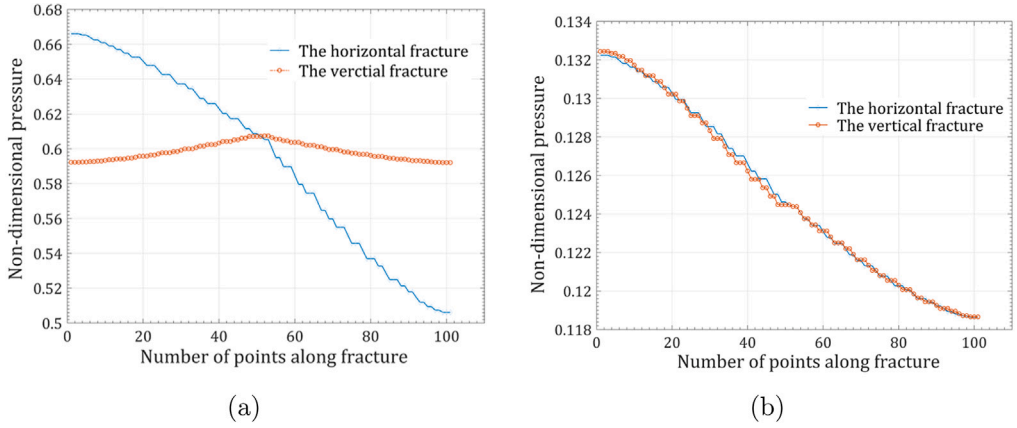

Fig. 11. Pressure variation along fractures when fractures are conductive pathway ($k_r = 10^5$). Note that (a) and (b) correspond to Figs. 9b and 9d, respectively.

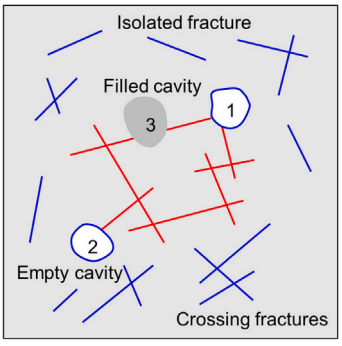

Fig. 12. Schematic of a porous medium with stochastic fractures and cavities.

cavity is set to $k_c/k_m = 1$. The fracture network highlighted in red color, as shown in Fig. 12, has different hydraulic property compared to the rock matrix. As indicated in Table 1, the permeability of the fracture network is assigned to $k_f/k_m = 10^{-5}$ and 10^5 in Patterns A and B, respectively. Therefore, the effects of impermeable and conductive pathway of the fracture network are simulated.

The simulation results are shown in Fig. 13. The injection is imposed on the left boundary $p_L = 1$MPa, while the outlet is placed on the right boundary. The presence of fracture network strongly influences the pressure distribution. It can be observed that a pressure concentration phenomenon is produced by the impermeable fractures ($k_f = 10^{-15}$ m^2) in Pattern A. The impact of the fracture network in Pattern B

Table 1
Model parameters in simulation.

	Pattern A	Pattern B	Pattern C
Matrix permeability k_m [m^2]	10^{-12}	10^{-12}	10^{-12}
Fracture aperture Δa [mm]	0.1	0.1	0.1
Fracture permeability k_f [m^2]	10^{-17}	10^{-5}	10^{-17}
Cavity permeability k_c [m^2]	10^{-12}	10^{-12}	10^{-15}
Empty cavity 1	–	–	Inlet
Empty cavity 2	–	–	Outlet
Pressure injection [MPa]	$p_L = 1$	$p_L = 1$	$p_c = 1$

is relatively small compared to Pattern A due to the fact that the conductive pathway directly conducts fluid through the fractures.

The impact of the impermeable and conductive fracture network can be further illustrated by the pressure variation along a monitoring line. A horizontal line is placed along this domain from coordinates $(0, 50)$ to $(100, 50)$, as depicted in Fig. 14. As shown in this figure, the pressure variation in Pattern A shows two significant jumps around the fracture network, which is marked by red color in Fig. 12. The first jump happens in the range 35∼40, and the second jump happens in range 60∼65. These two positions are coincidentally intersected by fractures. In Pattern A, the impermeable region in the center of the domain is constructed by the impermeable fracture network, which can be reflected in the pressure curve with range 40∼60. In contrast, the pressure variation in Pattern B shows a different tendency, in which the fracture network is assigned to a high-conductivity. Therefore, the tendency of pressure variation is smooth and monotonically decreases, which is consistent to the fact of the linear pressure gradient.

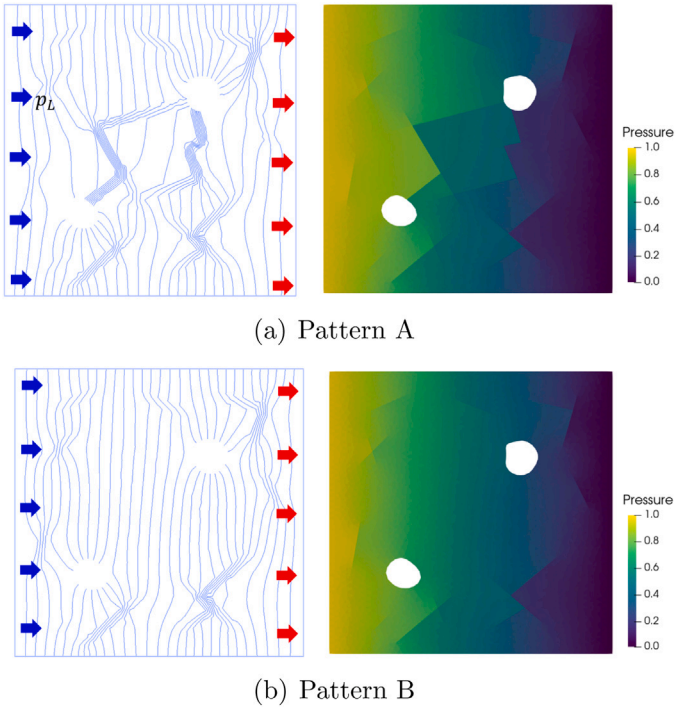

Fig. 13. Pressure distributions in Patterns A and B. The fracture network, highlighted in red color in Fig. 12, is assigned to $k_f/k_m = 10^{-5}$ and 10^5, respectively.

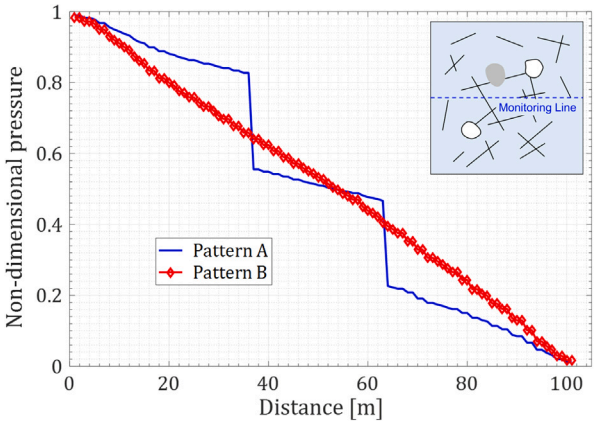

Fig. 14. Pressure variation along the monitoring line in Patterns A and B.

In contrast, this model is then simulated with Pattern C. The parameters are shown in Table 1. Boundary conditions, as well as the hydraulic conductivity of the cavities, are different from Patterns A and B. We consider different properties of the empty cavity (Cavities 1 and 2) and the filled cavity (Cavity 3), which are labeled in Fig. 12. The simulation results are displayed in Fig. 15. It shows that the low conductivity ($k_c = 10^{-15}$ m^2) of the filled cavity produces a relative low pressure region around Cavity 3. Fluid directly conducts from the source (Cavity 1) to the sink (Cavity 2), and then gathering in the region surrounded by the fracture network, as displayed in Fig. 12. The fracture network creates a connected pathway, therefore the conductive channel connects the cavities and the fracture–cavity network. Fig. 15 depicts the pressure field in the discrete fractures. Pressure decay along the fracture network is observed due to the pressure gradient generated by the pressure difference between the inlet and outlet.

5.4. The influence of heterogeneity on fluid flow

In practice, the geological field shows a random distribution of hydraulic property spatially. In different regions of a fractured reservoir, the permeability can be assigned to various magnitudes and the distribution may follow statistical laws. In contrast to the homogeneous assumption, in this section, we study the effect of heterogeneity on fluid flow. To this end, permeability field is generated randomly and is allowed to be changed in a range. The permeability distribution follows the statistical laws, such as the log-normal distribution (Wang et al., 2014; Cusini et al., 2018). In this work, the Gaussian distribution law is applied to create the heterogeneity in permeability field. As display in Fig. 16, the range of the matrix permeability can be changed between $0.7\sim1.2\times10^{-12}$ m^2. Other parameters are same as the above test.

Obviously, the heterogeneity influences the pressure distribution, as shown in Figs. 17 and 18. A comparison between the solutions of homogeneous and heterogeneous situations is provided. This impact is also related to the fracture permeability. It demonstrates that the impact of heterogeneity in low-conductivity fracture is relatively larger

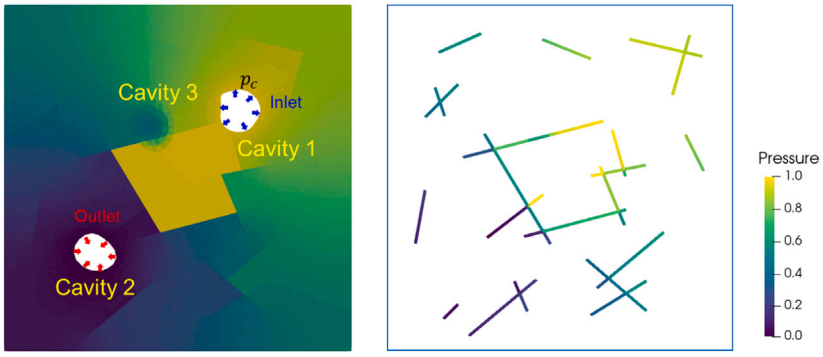

Fig. 15. Pressure distribution of the fractured porous medium in Pattern C.

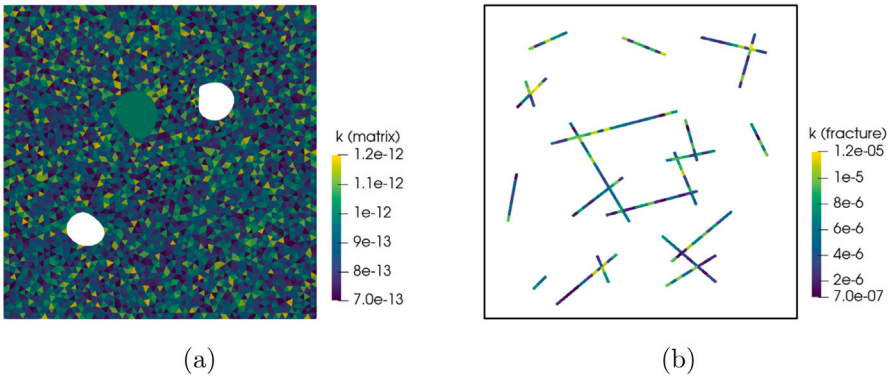

Fig. 16. Permeability distribution (unit: [m^2]) of the rock matrix (a) and fractures (b) with high-conductivity.

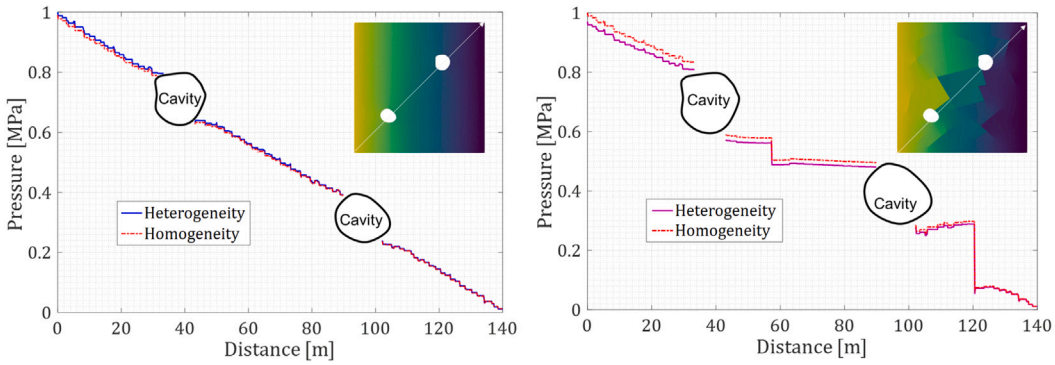

Fig. 17. Pressure variation along a monitoring line in the situations of low-conductivity (left) and high-conductivity (right) of fractures.

Table 2
Model parameters of the large-scale simulation.

Parameters	Values
Domain size	500 m × 250 m
Matrix permeability k_m	3.7×10^{-12}~2×10^{-8} m^2
Cavity permeability k_c	3.7×10^{-18}, 3.7×10^{-14} m^2
Fracture aperture Δa	0.1 mm
Fracture permeability k_f	3.7×10^{-17}~3.7×10^{-7} m^2
Inlet	p_L = 20 MPa
Outlet	p_R = 10 MPa

than the high-conductivity. Fig. 18 provides the pressure deviation induced by the heterogeneity. It is measured by the difference between the results of homogeneous and heterogeneous situations, defined as $\Delta p = |p^{ho} - p^{he}|$. The percentage of pressure deviation is defined by $\Delta p/p^{ho}$. The variation of pressure deviation along the diagonal of the domain is shown in Fig. 18. It indicates that the pressure deviation concentrates at the positions which are intersected by fractures. Especially, Δp is more significant around the discrete fractures if these fractures play the role of barriers. The reason is that the impermeable fractures may lead to a relative large deviation due to these fractures block fluid flow.

To investigate the effects of multiple cavities and fractures, as well as their hydraulic properties, on fluid flow, a large-scale fractured porous medium with heterogeneity is simulated, as shown in Fig. 19a. It can be seen that fractures and cavities are connected, therefore a fracture–cavity network is created. Boundary conditions and model parameters are shown in Table 2. We generate a random permeability field, as displayed in Fig. 19b. The permeability of cavities is allowed to be changed. The presence of cavities affects the flow pattern in this fractured medium. The filled cavities are equivalent to the barriers if the low-conductivity is used, as displayed in Fig. 21b. Otherwise, the cavities are permeable if a high-conductivity is used, such that fluid directly conducts through the fracture–cavity network.

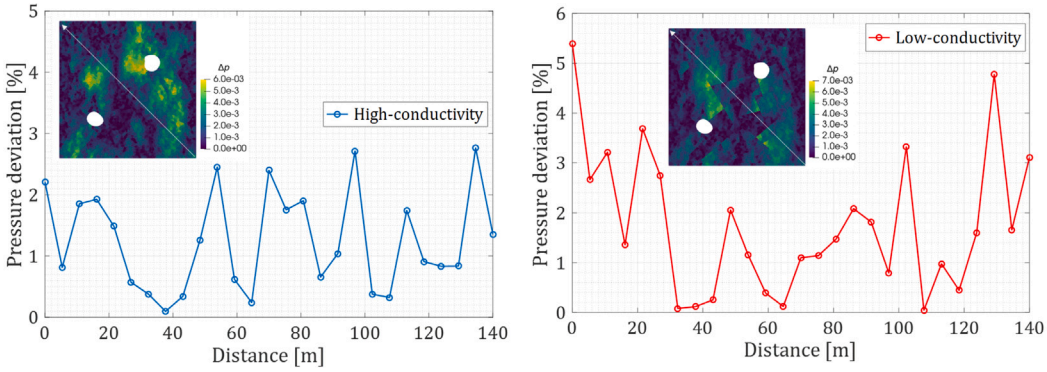

Fig. 18. Percentage of pressure deviation induced by heterogeneity measured by the difference between homogeneous and heterogeneous solutions.

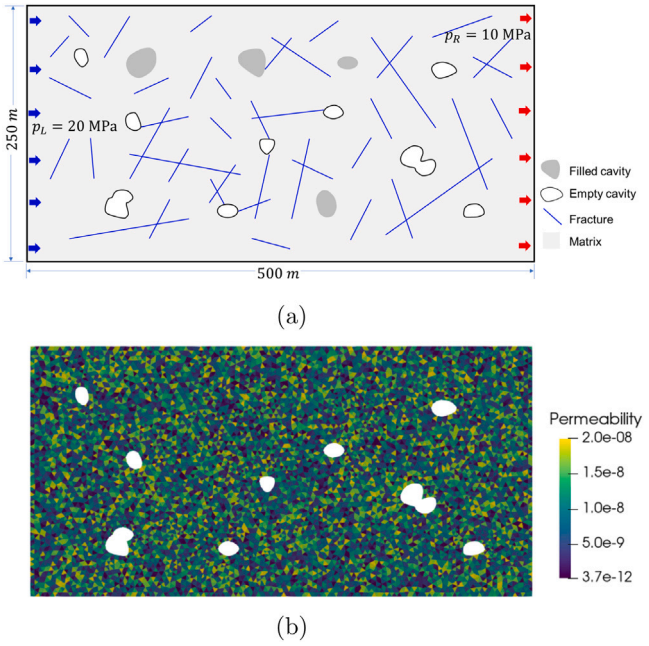

Fig. 19. The large-scale fractured porous medium. (a) Geometry of the model. (b) Permeability distribution (unit: m^2).

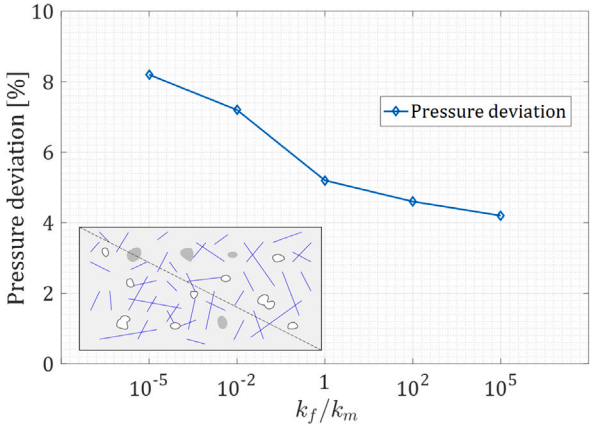

Fig. 20. Percentage of pressure deviation induced by heterogeneity with different permeabilities.

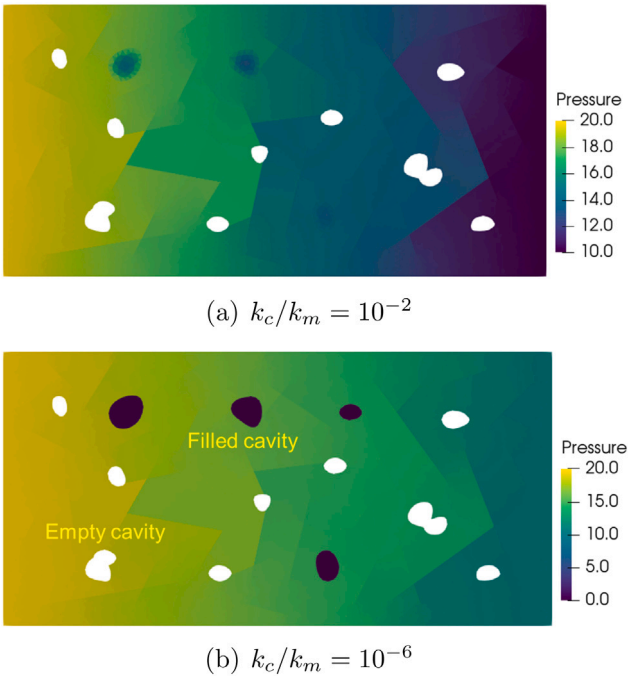

Fig. 21. Pressure distribution under different conditions (unit: MPa). (a) High-conductivity of the filled cavities. (b) Low-conductivity of the filled cavities (modeled as barriers).

Furthermore, the impact of heterogeneity on fluid flow is analyzed with different fracture permeability. As displayed in Fig. 20, the percentage of pressure deviation $\Delta p/p^{ho}$, induced by the random permeability field, is calculated by the difference between the solutions of homogeneous and heterogeneous situations. It appears that this value decreases with the increase of fracture permeability. Therefore, it indicates that the influence of heterogeneity on high-conductivity fractures is relatively smaller than the low-conductivity.

6. Conclusions

This work presents a numerical investigation on fluid flow in heterogeneous porous media, in which the influence of discrete fractures and cavities with different conductivities is simulated. A hybrid-dimensional modeling approach combined with the dual fracture-pore model is presented. Based on these, the effects of fracture–cavity network, as well as hydraulic property, on fluid flow are studied.

The numerical method is based on the Galerkin finite element method, in which the shape function is selected as a piece-wise constant function. The discrete fractures are discretized as the low-order objects compared to the rock matrix cells, while the natural cavities are modeled and categorized into filled and empty cavities. The numerical

treatment of flux connection of multiple fractures is elaborated. Specially, the connections of fractures–fractures and matrix–fractures are resolved by the classification of different types of cell, therefore the high-dimensional cells (matrix and cavities) and the low-dimensional cells (fractures) are considered in different situations.

A series of numerical tests is conducted to verify the presented method and to investigate pressure distribution in fractured porous media under different conditions. First, the results calculated by different grid resolutions are compared with the reference solution. A grid convergence test is performed to show the grid independence. Then, a sensitivity study is conducted to investigate the impacts of boundary conditions and fracture permeability on pressure distribution. The fractures are allowed to be modeled as barriers or conductive pathways. Next, a fractured porous medium with different types of cavity is simulated with the consideration of flux connection in fracture–cavity network. The effects of impermeable and conductive fractures on fluid flow are analyzed. Later, in contrast to the homogeneous situation, we study the effect of heterogeneity on fluid flow. Pressure deviation induced by heterogeneity is investigated with different permeabilities of fractures and cavities.

Several extensions of the presented study deserve a further investigation. Typically, the fractured vuggy porous media, with multiple scale fractures and cavities, is widely existing in carbonate reservoir engineering. However, it is impossible to simulate all the multiple scale fractures and cavities due to the computational cost. Developing an upscaling approach and then combining with our numerical method is an efficient strategy.

CRediT authorship contribution statement

Luyu Wang: Conceptualization, Methodology, Software, Funding acquisition, Writing – original draft. **Weizhong Chen:** Supervision, Funding acquisition, Writing – review & editing. **Cornelis Vuik:** Supervision, Methodology, Validation, Writing – review & editing.

Declaration of competing interest

The authors declare that they have no known competing financial interests or personal relationships that could have appeared to influence the work reported in this paper.

Acknowledgments

This work was financially supported by China Scholarship Council (grant number 201904910310) and National Natural Science Foundation of China (grant number 51991392). Luyu Wang thanks the discussion and advice from colleagues in ADMIRE group and DIAM of TU Delft.

References

Ababou, R., McLaughlin, D., Gelhar, L.W., Tompson, A.F.B., 1989. Numerical simulation of three-dimensional saturated flow in randomly heterogeneous porous media. Transp. Porous Media 4, 549–565. http://dx.doi.org/10.1007/BF00223627.

Atashbeyk, M.Dabiri., Shahbazi, K., Fattahi, M., 2018. Pressure profile estimation through CFD in UBD operation considering with influx to wellbore. Iran. J. Chem. Chem. Eng 37 (6), 271–283.

Bahrainian, S.S., Dezfuli, A.Daneh., Noghrehabadi, A., 2015. Unstructured grid generation in porous domains for flow simulations with discrete-fracture network model. Transp. Porous Media 109, 693–709. http://dx.doi.org/10.1007/s11242-015-0544-3.

Berkowitz, B., 2002. Characterizing flow and transport in fractured geological media: A review. Adv. Water Resour. 25, 861–884. http://dx.doi.org/10.1016/S0309-1708(02)00042-8.

Berrone, S., Pieraccini, S., Scialò, S., 2013. A PDE-constrained optimization formulation for discrete fracture network flows. SIAM J. Sci. Comput. 35, B487–B510. http://dx.doi.org/10.1137/120865884.

Cacas, M.C., Ledoux, E., Marsily, G.de., Tillie, B., Barbreau, A., Durand, E., Feuga, B., Peaudecerf, P., 1990. Modeling fracture flow with a stochastic discrete fracture network: calibration and validation: 1. Flow Model. Water Resour. Res. 26, 479–489. http://dx.doi.org/10.1029/WR026i003p00479.

Cappa, F., Rutqvist, J., 2011. Modeling of coupled deformation and permeability evolution during fault reactivation induced by deep underground injection of CO2. Int. J. Greenh. Gas Control 5, 336–346. http://dx.doi.org/10.1016/j.ijggc.2010.08.005.

Cusini, M., Fryer, B., Kruijsdijk, C.van., Hajibeygi, H., 2018. Algebraic dynamic multilevel method for compositional flow in heterogeneous porous media. J. Comput. Phys. 354, 593–612. http://dx.doi.org/10.1016/j.jcp.2017.10.052.

Dietrich, P., Helmig, R., Sauter, M., Teutsch, G., Hötzl, H., Köngeter, J., 2005. Flow and Transport in Fractured Porous Media. Springer-Verlag, Berlin Heidelberg, http://dx.doi.org/10.1007/b138453.

Eymard, R., Gallouët, T., Herbin, R., 2000. Finite Volume Methods. Handbook of Numerical Analysis, Volume 7. Elsevier, pp. 713–1018. http://dx.doi.org/10.1016/S1570-8659(00)07005-8.

Fumagalli, A., Keilegavlen, E., Scialò, S., 2019. Conforming, non-conforming and non-matching discretization couplings in discrete fracture network simulations. J. Comput. Phys. 376, 694–712. http://dx.doi.org/10.1016/j.jcp.2018.09.048.

Gerke, H.H., van Genuchten, M.T., 1993. A dual-porosity model for simulating the preferential movement of water and solutes in structured porous media. Water Resour. Res 29, 305–319. http://dx.doi.org/10.1029/92WR02339.

Graf, T., Therrien, R., 2008. A method to discretize non-planar fractures for 3D subsurface flow and transport simulations. Internat. J. Numer. Methods Fluids 56, 2069–2090. http://dx.doi.org/10.1002/fld.1607.

Hadgu, T., Karra, S., Kalinina, E., Makedonska, N., Hyman, J.D., Klise, K., Viswanathan, H.S., Wang, Y., 2017. A comparative study of discrete fracture network and equivalent continuum models for simulating flow and transport in the far field of a hypothetical nuclear waste repository in crystalline host rock. J. Hydrol. 553, 59–70. http://dx.doi.org/10.1016/j.jhydrol.2017.07.046.

Hajibeygi, H., Jenny, P., 2011. Adaptive iterative multiscale finite volume method. J. Comput. Phys. 230, 628–643. http://dx.doi.org/10.1016/j.jcp.2010.10.009.

Hajibeygi, H., Karvounis, D., Jenny, P., 2011. A hierarchical fracture model for the iterative multiscale finite volume method. J. Comput. Phys. 230, 8729–8743. http://dx.doi.org/10.1016/j.jcp.2011.08.021.

Hosseini-Ardali, S.M., Hazrati-Kalbibaki, M., Fattahi, M., Lezsovits, F., 2020. Multi-objective optimization of post combustion CO2 capture using methyldiethanolamine (MDEA) and piperazine (PZ) bi-solvent. Energy 211 (15), 119035. http://dx.doi.org/10.1016/j.energy.2020.119035.

HosseiniMehr, M., Cusini, M., Vuik, C., Hajibeygi, H., 2018. Algebraic dynamic multilevel method for embedded discrete fracture model (f-ADM). J. Comput. Phys. 373, 324–345. http://dx.doi.org/10.1016/j.jcp.2018.06.075.

Huang, N., Liu, R., Jiang, Y., Cheng, Y., 2021a. Development and application of three-dimensional discrete fracture network modeling approach for fluid flow in fractured rock masses. J. Nat. Gas Sci. Eng. 103957. http://dx.doi.org/10.1016/j.jngse.2021.103957.

Huang, X., Zhang, L., Zhang, R., Chen, X., Zhao, Y., Yuan, S., 2021b. Numerical simulation of gas-liquid two-phase flow in the micro-fracture networks in fractured reservoirs. J. Nat. Gas Sci. Eng 94, 104101. http://dx.doi.org/10.1016/j.jngse.2021.104101.

Hyman, J.D., Gable, C.W., Painter, S.L., Makedonska, N., 2014. Conforming delaunay triangulation of stochastically generated three dimensional discrete fracture networks: A feature rejection algorithm for meshing strategy. SIAM J. Sci. Comput 36, A1871–A1894. http://dx.doi.org/10.1137/130942541.

Hyman, J.D., Karra, S., Makedonska, N., Gable, C.W., Painter, S.L., Viswanathan, H.S., 2015. Dfnworks: A discrete fracture network framework for modeling subsurface flow and transport. Comput. Geosci. 84, 10–19. http://dx.doi.org/10.1016/j.cageo.2015.08.001.

Jha, B., Juanes, R., 2007. A locally conservative finite element framework for the simulation of coupled flow and reservoir geomechanics. Acta. Geotech. 2, 139–153. http://dx.doi.org/10.1007/s11440-007-0033-0.

Jing, L., 2003. A review of techniques, advances and outstanding issues in numerical modelling for rock mechanics and rock engineering. Int. J. Rock Mech. Min. Sci. 40, 283–353. http://dx.doi.org/10.1016/S1365-1609(03)00013-3.

Karimi-Fard, M., Durlofsky, L.J., Aziz, K., 2004. An efficient discrete-fracture model applicable for general-purpose reservoir simulators. SPE J. 9, 227–236. http://dx.doi.org/10.2118/88812-PA.

King, P.R., 1989. The use of renormalization for calculating effective permeability. Transp. Porous Media 4, 37–58. http://dx.doi.org/10.1007/BF00134741.

Lang, P.S., Paluszny, A., Zimmerman, R.W., 2014. Permeability tensor of three-dimensional fractured porous rock and a comparison to trace map predictions. J. Geophys. Res. Solid Earth 119, 6288–6307. http://dx.doi.org/10.1002/2014JB011027.

Layton, W.J., Schieweck, F., Yotov, I., 2002. Coupling fluid flow with porous media flow. SIAM J. Numer. Anal 40, 2195–2218. http://dx.doi.org/10.1137/S0036142901392766.

LeVeque, R.J., 1992. Numerical Methods for Conservation Laws. Birkhäuser, Basel.

Long, J.C.S., Billaux, D.M., 1987. From field data to fracture network modeling: An example incorporating spatial structure. Water Resour. Res. 23, 1201–1216. http://dx.doi.org/10.1029/WR023i007p01201.

Moradi, F., Kazemeini, M., Fattahi, M., 2014. A three dimensional CFD simulation and optimization of direct DME synthesis in a fixed bed reactor. Pet. Sci. 11, 323–330. http://dx.doi.org/10.1007/s12182-014-0347-0.

Mustapha, H., Dimitrakopoulos, R., Graf, T., Firoozabadi, A., 2011. An efficient method for discretizing 3D fractured media for subsurface flow and transport simulations. Internat. J. Numer. Methods Fluids 67, 651–670. http://dx.doi.org/10.1002/fld.2383.

Nie, R.S., Meng, Y.F., Jia, Y.L., Zhang, F.X., Yang, X.T., Niu, X.N., 2012. Dual porosity and dual permeability modeling of horizontal well in naturally fractured reservoir. Transp. Porous Media 92, 213–235. http://dx.doi.org/10.1007/s11242-011-9898-3.

Ratnakar, R.R., Dindoruk, B., Harvey, A., 2020. Thermodynamic modeling of hydrogen-water system for high-pressure storage and mobility applications. J. Nat. Gas Sci. Eng. 81, 103463. http://dx.doi.org/10.1016/j.jngse.2020.103463.

Rutqvist, J., Birkholzer, J.T., Tsang, C.F., 2008. Coupled reservoir-geomechanical analysis of the potential for tensile and shear failure associated with CO2 injection in multilayered reservoir-caprock systems. Int. J. Rock Mech. Min. Sci 45, 132–143. http://dx.doi.org/10.1016/j.ijrmms.2007.04.006.

Shakiba, M., Cavalcante Filho, A., Sepehrnoori, K., 2018. Using embedded discrete fracture model (EDFM) in numerical simulation of complex hydraulic fracture networks calibrated by microseismic monitoring data. J. Nat. Gas Sci. Eng. 55, 495–507. http://dx.doi.org/10.1016/j.jngse.2018.04.019.

Sherratt, J., Haddad, A.Sharifi., Rafati, R., Manzari, M.T., 2020. A fracture upscaling method (FUM) for hydraulically fractured reservoirs: From discrete fracture modelling to finite difference simulations. J. Nat. Gas Sci. Eng. 83, 103611. http://dx.doi.org/10.1016/j.jngse.2020.103611.

Stefansson, I., Berre, I., Keilegavlen, E., 2018. Finite-volume discretisations for flow in fractured porous media. Transp. Porous Media 124, 439–462. http://dx.doi.org/10.1007/s11242-018-1077-3.

Tan, X., Chen, W., Wang, L., Yang, J., Tan, X., 2020. Settlement behaviors investigation for underwater tunnel considering the impacts of fractured medium and water pressure. Mar. Georesources Geotechnol. 39 (6), 639–648. http://dx.doi.org/10.1080/1064119X.2020.1737279.

Ţene, M., Bosma, S.B.M., Al Kobaisi, M.S., Hajibeygi, H., 2017. Projection-based embedded discrete fracture model (pEDFM). Adv. Water Resour. 105, 205–216. http://dx.doi.org/10.1016/j.advwatres.2017.05.009.

Wang, L., Chen, W., Tan, X., Tan, X., Yang, J., Yang, D., Zhang, X., 2020. Numerical investigation on the stability of deforming fractured rocks using discrete fracture networks: a case study of underground excavation. Bull. Eng. Geol. Environ. 79, 133–151. http://dx.doi.org/10.1007/s10064-019-01536-9.

Wang, L., Chen, W., Tan, X., Tan, X., Yuan, J., Liu, Q., 2019a. Evaluation of mountain slope stability considering the impact of geological interfaces using discrete fractures model. J. Mt. Sci. 16, 2184–2202. http://dx.doi.org/10.1007/s11629-019-5527-3.

Wang, L., Chen, W., Tan, X., Yang, J., 2019b. The impact of various crack geometrical parameters on stress field over tip under different mixed loading conditions and inclination angles. Theor. Appl. Fract. Mech. 102, 239–254. http://dx.doi.org/10.1016/j.tafmec.2018.12.001.

Wang, Y., Hajibeygi, H., Tchelepi, H.A., 2014. Algebraic multiscale solver for flow in heterogeneous porous media. J. Comput. Phys. 259, 284–303. http://dx.doi.org/10.1016/j.jcp.2013.11.024.

Wei, S., Jin, Y., Xia, Y., 2020. Predict the mud loss in natural fractured vuggy reservoir using discrete fracture and discrete vug network model. J. Pet. Sci. Eng. 195, 107626. http://dx.doi.org/10.1016/j.petrol.2020.107626.

Yao, J., Huang, Z., Li, Y., Wang, C., Lv, X., 2010. Discrete fracture-vug network model for modeling fluid flow in fractured vuggy porous media. In: Society of Petroleum Engineers - International Oil and Gas Conference and Exhibition in China 2010. IOGCEC, 32, pp. 0–333. http://dx.doi.org/10.2118/130287-ms.

Zhang, H., Sheng, J.J., 2021. An efficient embedded discrete fracture model based on the unstructured quadrangular grid. J. Nat. Gas Sci. Eng. 103710. http://dx.doi.org/10.1016/j.jngse.2020.103710.

Zhang, N., Yao, J., Xue, S., Huang, Z., 2016. Multiscale mixed finite element, discrete fracture-vug model for fluid flow in fractured vuggy porous media. Int. J. Heat Mass Transfer 96, 396–405. http://dx.doi.org/10.1016/j.ijheatmasstransfer.2015.11.090.

Zienkiewicz, O., Taylor, R., Zhu, J.Z., 2013. The Finite Element Method: Its Basis and Fundamentals, Seventh ed. Elsevier, http://dx.doi.org/10.1016/C2009-0-24909-9.